Aging behavior of Cu–Ti–Al alloy observed by transmission electron microscopy

Toyohiko J. Konno · Rimi Nishio · Satoshi Semboshi ·
Tetsu Ohsuna · Eiji Okunishi

Abstract Aging behavior of Cu–3 at.%Ti–4 at.%Al alloy at 723 K has been examined from mechanical, electrical, and microstructural points of view. Compared with binary Cu–3 at.%Ti alloy, the electrical conductivity improved six times to about 6%IACS (international annealed copper standard); whereas the peak hardness decreased from 280 to 180 Hv. The major strengthening phase is the tetragonal α-Cu_4Ti, which forms not via spinodal decomposition but based on the nucleation and growth mechanism. The precipitates grow in the c direction of the tetragonal phase, which lies along one of the $\langle 100 \rangle$ axes of the matrix fcc Cu phase. This growth mode minimizes the strain energy arising from the lattice mismatch of about 2% between the matrix and precipitate; and results in a square rod shape, which reaches about 50 nm in length after 100 h anneal. Another precipitating phase is $AlCu_2Ti$ ($D0_3$, Strukturbericht notation), with the major habit plane

T. J. Konno (✉)
Institute of Materials Research, Tohoku University,
2-1-1 Katahira, Aoba-Ku, Sendai 980-8577, Japan
e-mail: tjkonno@imr.tohoku.ac.jp

R. Nishio · S. Semboshi
Department of Materials Science, Osaka Prefecture University,
1-1 Gakuencho, Naka-Ku, Sakai 599-8531, Japan

Present Address:
R. Nishio
Ibiden Co., Ltd., 2-1 Kanda-cho, Ogaki, Gifu 503-8604, Japan

T. Ohsuna
Kagami Memorial Laboratory for Materials Science
and Technology, Waseda University, 2-8-26 Nishi-Waseda,
Shinjuku-Ku, Tokyo 169-0051, Japan

E. Okunishi
JEOL Ltd., 3-1-2 Musashino, Akishima, Tokyo 196-8558, Japan

close to {110} of the fcc Cu matrix. The orientation relationship was not definitely determined, but it was found that the angle between the 100 and 110 poles of the matrix and precipitates, respectively, is about 5°, while the angle between the two 001 axes being about 7°. It was suggested that the formation of this ternary phase reduced the solute Ti concentration, leading to the decrease in the resistivity.

Introduction

Age-hardened Cu-based alloys are indispensable for electrical connection, and among them, the Cu–Be alloys exhibit by far the optimum balance of mechanical strength and electrical conductivity [1, 2]. Recently, however, much effort has been put forward in order to replace the Cu–Be alloys because of their environmental hazards. From materials science points of view, the necessity to provide toxic-free materials has aroused renewed interests in the decomposition and age-hardening mechanism in the Cu–Ti-based systems [3–7]. As exemplified earlier, the peak hardness is provided basically by the fine distribution of the intermetallic compound, α-Cu_4Ti [8], which has the $D1_a$ (in Strukturbericht designation) or Ni_4Mo structure ($I4/m$, $a = 0.584$ nm, $c = 0.362$ nm) [9, 10]. The fine distribution is best provided by the spinodal decomposition, which takes place when the amount of Ti exceeds 2–3 at.%. On the contrary, when the amount of Ti is not enough for the spinodal reaction, the α-Cu_4Ti phase emerges via the nucleation and growth mechanism, resulting in a rather sparse distribution of the α-Cu_4Ti precipitates [11–13].

From practical points of view, the presence of solute Ti atoms results in unavoidable increase in the resistivity. The contributions of some of the elements to the

resistivity of pure Cu are known to be, for example, 0.14×10^{-8} Ω m/at.% for Ag, 0.62 for Be, 1.25 for Al, 6.35 for Co, and ≈ 12 for Ti. The notable effect of Ti originates from the fact that the d-states provided by Ti are progressively occupied by the electron transfer from Cu, which results in the net decrease of carrier density. Thus, one logical way to improve the electrical conductivity in the binary Cu–Ti system is to reduce the solute Ti, while maintaining the precipitation of the α-Cu_4Ti phase. We intended to achieve this goal by adding a third element which will "trap" the solute Ti, while presumably leaving the precipitation of α-Cu_4Ti unchanged.

In the present article, we extend our previous work on the Cu–3 at.%Ti alloy, in which microstructural changes in this alloy, observed by transmission electron microscopy (TEM), have been described in detail [7]; and report the effect of adding Al to the binary Cu–Ti system. According to the Cu–Ti–Al ternary phase diagram [10, 14], an addition of moderate amount of Al does not remove the α-Cu_4Ti phase, but results in a state of three phase equilibrium among the face-centered cubic (fcc)-Cu, α-Cu_4Ti, and $AlCu_2Ti$ phases. The latter is an intermetallic compound with the $D0_3$ or BiF_3 structure ($a = 0.601$ nm), in which Al and Ti atoms occupy the fcc lattice and octahedral sites, respectively, whereas Cu atoms occupy the tetrahedral sites [15]. The purpose of the present investigation was thus to examine the effect of Al addition, and shed light on the aging behavior of Cu–Ti–Al alloys by mechanical and electrical measurements, and by structural observation using TEM.

Experimental procedure

Button ingots of Cu–Ti and Cu–Ti–Al alloys were prepared by arc-melting in an argon atmosphere, using 99.99% copper, titanium and/or, aluminum as starting materials. The chemical composition of the alloys were determined to be Cu–3.0 at.%Ti and Cu–3.0 at.%Ti–4.0 at.%Al by inductively coupled plasma spectroscopy. The ingots were cut into blocks, which were then solution-treated at 1,173 K for 2 h and quenched in ice water. Immediately after quenching, they were aged at 723 K for 2, 4, 8, 40, and 100 h in an argon atmosphere. The TEM samples were cut from the block and electropolished in 80% methanol and 20% nitric acid solution at 223 K using a twin jet electropolishing machine. We used a JEM-2000FX operating at 200 kV for preliminary TEM observation, while JEM-3000F at 300 kV and JEM-2100F at 200 kV were utilized for HRTEM (high-resolution TEM) and STEM (scanning TEM) investigations. Diffraction patterns in this report are presented after proper rotation calibration unless otherwise stated.

Experimental results

Figure 1a compares changes in Vicker's hardness of the Cu–3 at.%Ti–4 at.%Al alloy aged at 723 K to those of Cu–3 at.%Ti alloy. In the Cu–Ti binary alloy, the hardness reached its maximum of about 280 Hv at 8 h of annealing, whereas in the Cu–Ti–Al alloy, the maximum value was 180 Hv, which appeared at 2 h. Figure 1b is a similar comparison for electrical conductivity, expressed in terms of %IACS (international annealed copper standard). As seen, the conductivity of the Cu–Ti alloy show a gradual increase in the region less than 2%IACS, while that of the Cu–Ti–Al exhibit an immediate increase to a value of nearly 6%IACS, followed by a slight decrease.

Figure 2a is a BF image of the as-quenched Cu–3 at.% Ti–4 at.%Al alloy viewed approximately along the [110] zone axis, showing quenched-in dislocations. Figure 2b (inset) is also a BF image of the same specimen viewed along the [100] zone axis, where contrast arising from a strain field of about 4 nm is apparent. Note that some of the contrast features are planar, while the others are linear, in the plane
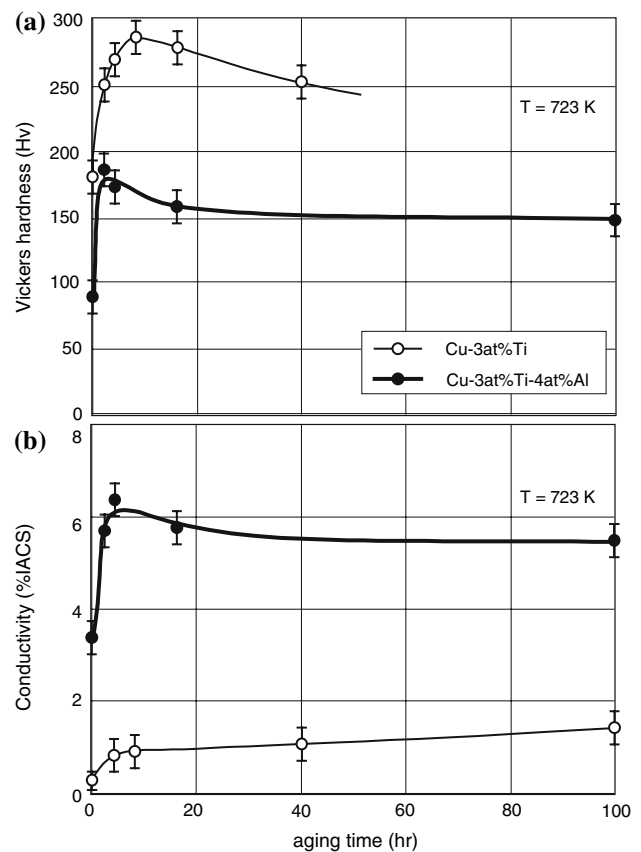

Fig. 1 Changes in mechanical and electrical properties of the Cu–3 at.%Ti and Cu–3 at.%Ti–4 at.%Al alloys aged at 723K. (**a**) Vickers hardness, (**b**) electrical conductivity. The latter is expressed in terms of %IACS, the percentile of the resistivity with respect to that of the pure Cu
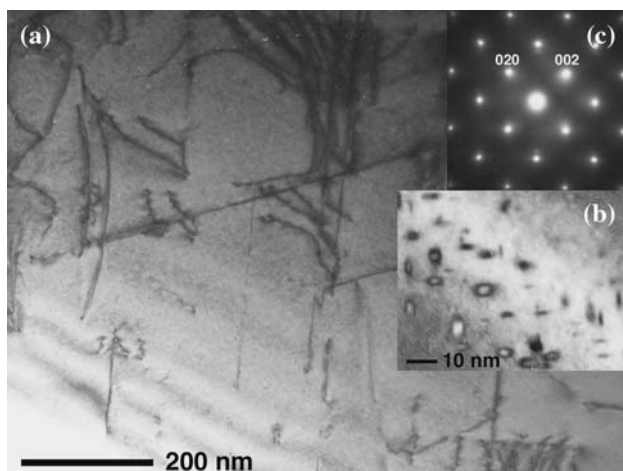
Fig. 2 BF images and SAD pattern of the as-quenched Cu–3 at.%Ti–4 at.%Al alloy. (**a**) Low-magnification BF image, viewed along the [110] zone axis, showing quenched-in dislocations; (**b**) BF image at a higher magnification, viewed along the [100] zone axis, showing contrasts of about 4 nm arising from a strain field; (**c**) SAD pattern taken from the region shown in (**b**)

normal to ⟨110⟩ directions of the matrix. Figure 2c is a selected area diffraction (SAD) pattern taken from the region shown in (b). As seen, this pattern is simply the one expected from the Cu matrix (minor spot along the 022 spot is due to Cu oxides). We examined this as-quenched specimen using STEM, together with characteristic X-ray mapping (similar to Fig. 6), but found no elemental redistribution that might have caused the strain contrast.

Figure 3 is a BF image of the Cu–3 at.%Ti–4 at.%Al alloy, annealed at 723K for 2 h, and an inset SAD pattern, viewed along [001] zone axis (slightly overexposed in order to emphasize superlattice spots). As seen, the image
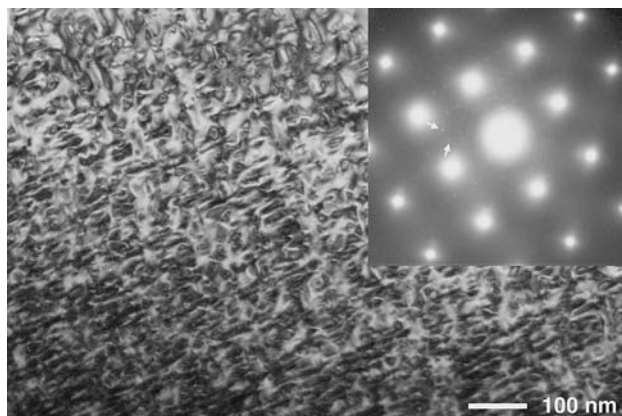

Fig. 3 BF image of the Cu–3 at.%Ti–4 at.%Al alloy, annealed at 723K for 2 h, showing strain contrasts arising from precipitates of approximately 50 nm in length, and inset [001] SAD pattern. Note the presence of superlattice spots at 1/5 420 and its equivalent positions, as indicated by arrows, suggesting the formation of the α-Cu_4Ti phase

is dominated by strain contrasts of approximately 50 nm in length. The diffraction pattern exhibits weak superlattice spots at 1/5 420 and its equivalent positions, some of which are indicated by arrows. These spots are those expected from the 001 diffraction pattern of the $D1_a$ structure, and thus demonstrate that the α-Cu_4Ti phase has formed with the orientation relationship (OR) of $[001]_{fcc}//[001]_\alpha$, $(310)_{fcc}//(100)_\alpha$.

Figure 4a is a BF image of Cu–3 at.%Ti–4 at.%Al alloy annealed for 100 h. It can be seen that precipitates grew to a size of 200 nm in length. With the aforementioned OR and unit cell parameters of the fcc Cu and α-Cu_4Ti phases, it is expected that the latter is perfectly coherent in the c direction, but expands by 2% in the a directions of the tetragonal unit cell. The fact that moiré patterns are visible along the rod direction of the precipitates thus immediately suggests that these precipitates grew in the c direction, which lie perpendicular to the incident electron beam. The inset SAD pattern was obtained in the region indicated by the circle in the figure. The position of superlattice spots is now asymmetrical with respect to the spots arising from fcc Cu, showing that the precipitate is in fact composed of single domain. The morphology of these precipitates suggests that they assume a square rod shape with {100} habit planes. Figure 4b and c are STEM–HAADF (high-angle annular detector dark field) and STEM–BF images, respectively. These image can essentially be regarded as Z-contrast, reflecting the difference in atomic numbers, 22 and 29 for Ti and Cu. It is interesting to note that the distribution of the α-Cu_4Ti precipitates are far from random, but they tend to align along the ⟨100⟩ direction of the matrix.

Figure 5a is a low-magnification BF image of the same specimen. Apart from the α-Cu_4Ti precipitates described above, note the existence of large precipitates in the central region of the figure. Figure 5b is a SAD pattern taken from the precipitate. Some of the spots can be indexed as shown in the pattern, and the presence of weak spots at 002, 111, and their equivalent positions, suggests that it is the $[1\bar{1}0]$ diffraction pattern expected from the CaF_2 or BiF_3 structure. This strongly suggests that the large precipitate is indeed the $AlCu_2Ti$ phase. We also found that when the electron beam is along the [100] axis of the fcc matrix, one has to tilt the specimen slightly to align the precipitate along the [110] zone axis. For example, Fig. 5c is a diffraction pattern taken with an electron beam moderately converged as indicated in the figure, in order to obtain Kikuchi bands from the matrix and precipitate simultaneously. From this pattern, one can state that the 100 pole of the matrix and 110 pole of the precipitate are approximately 5.3° apart from each other.

Figure 6 is STEM–BF image and corresponding images are formed by characteristic X-rays taken simultaneously

Fig. 4 The Cu–3 at.%Ti–4 at.%Al alloy, annealed at 723 K for 100 h, viewed along the [001] zone axis. (**a**) BF image, showing contrasts arising from the α-Cu$_4$Ti precipitates of about 200 nm in length, lying in the $\langle 100 \rangle$ directions. The inset SAD pattern was taken from the encircled region. (**b**) STEM–HAADF and (**c**) STEM–BF images (at the same scale as in (**a**)), exhibiting the difference in Z in the matrix and precipitates
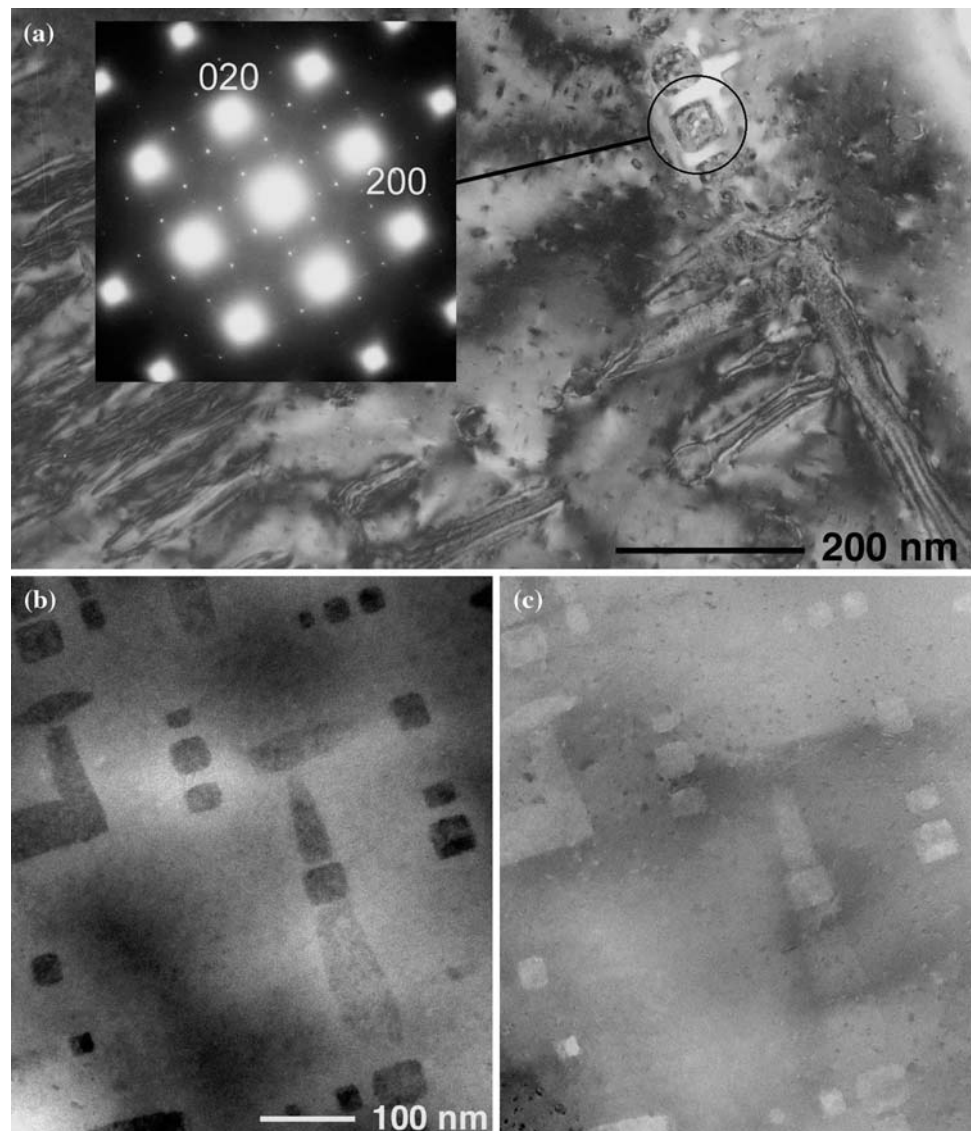
from the same specimen. One can see that Ti atoms are enriched both in the α-Cu$_4$Ti and AlCu$_2$Ti precipitates, while Al atoms are enriched in the latter only.

Figure 7a and b are STEM–BF image and characteristic X-ray profiles for Cu, Ti, and Al. The profiles were taken across the α-Cu$_4$Ti precipitate, as indicated in the figure. Although the Cu signals contain unavoidable background, the line profile still shows that the composition of Cu and Ti is close to 4:1, and the solubility of Al in the precipitate is very small. Figure 7c and d are a similar set of image and profile obtained for the AlCu$_2$Ti precipitate. The profile shows that the X-ray intensities from the precipitate are in a qualitative agreement with the stoichiometric composition, and that the solute Ti in the matrix is smaller than that of Al.

Figure 8a and b are atomic resolution STEM–HAADF and STEM–BF images, respectively, obtained simultaneously

from an interface region of the matrix (left) and the α-Cu$_4$Ti precipitate (right). The coherency of the two phases at the interface is evident. As for the interpretation of the image, it can be noticed that Ti atomic columns appear darker than Cu columns in HAADF, (a), while they appear brighter than the Cu columns in BF, (b). This reciprocity is in accordance with our intuitive DF–BF relation. However, notice also that the Cu columns appear bright both in HAADF and BF. That is, STEM–HAADF image is not a simple reverse contrast of STEM–BF, as it was roughly true for low-magnification contrasts, see Fig. 4b and c. Figure 8c is a HRTEM image obtained from a similar interface region in the same specimen. One notices that the contrast shown here is qualitatively similar to that of STEM–BF. This similarity manifests the theorem of reciprocity [16], and suggests that one has to take into account many beam effects in order to properly interpret
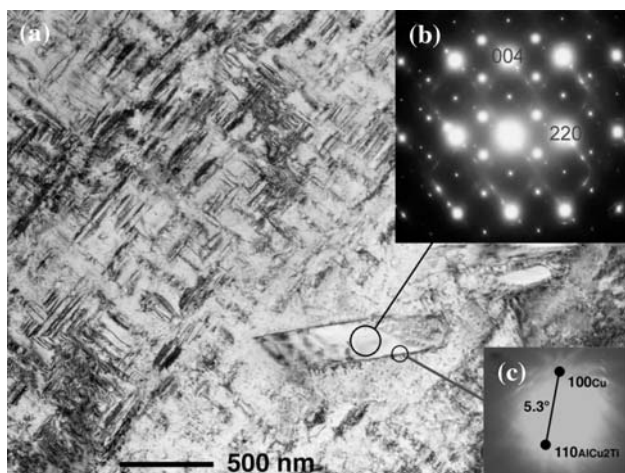
Fig. 5 (**a**) BF image of the Cu–3 at.%Ti–4 at.%Al alloy, annealed at 723 K for 100 h, viewed along the [100] zone axis. (**b**) SAD pattern obtained from the large particle shown in (**a**). (The pattern was taken by tilting the specimen about 5°) The pattern can be indexed according to the BiF$_3$ structure, showing that the large precipitate is the AlCu$_2$Ti phase. (**c**) Diffraction pattern taken with an electron beam slightly converged at the interface region as indicated in the figure, showing that the angle between 100 pole of the Cu matrix and 110 pole of the AlCu$_2$Ti precipitate is approximately 5.3°

the contrast of STEM–BF images, whereas that STEM–HAADF images can be regarded as Z-contrast.

Figure 9 is a HRTEM image of an interface region between the Cu matrix (upper) and the AlCu$_2$Ti precipitate (lower). This image was taken with the electron beam oriented along the [1$\bar{1}$0] zone axis of the precipitate. As described earlier in Fig. 5, the [100] zone axis of the matrix

and the [1$\bar{1}$0] of the precipitate are not parallel but tilted by about 5°; and thus the image of the matrix does not appear clearly as those in Fig. 8. Nevertheless by looking the interface at a glancing angle, the correspondence of the atomic planes across the interface is clear. For example, it can be seen that the [001] axis of fcc Cu is tilted with respect to that of AlCu$_2$Ti by approximately 7°, and a misfit dislocation arises every 10–20 (010) planes of the Cu matrix.

Discussion

We have shown that the addition of Al to the Cu–3 at.%Ti alloy has improved the conductivity, but at the same time it resulted in the decrease of mechanical hardness. The terminal microstructure was composed of the tetragonal α-Cu$_4$Ti and cubic AlCu$_2$Ti phases, in accordance with the equilibrium phase diagram [14]. Both of them are fully or at least partially coherent with the fcc Cu matrix.

It is known that the binary Cu–3 at.%Ti alloy spinodally decomposes upon quenching [7, 17, 18]. However, the present study showed that this is not the case for the ternary Cu–3 at.%Ti–4 at.%Al alloy. The BF image of the as-quenched specimen (Fig. 2) showed no contrast due to composition modulation, but it was dominated by dislocations and strain contrasts of about 4 nm. Since our chemical analysis was not able to detect a possible compositional variation around the strain contrasts within the present detection limit, and the SAD pattern showed no

Fig. 6 STEM–BF and simultaneous characteristic X-ray images of the Cu–3 at.%Ti–4 at.%Al alloy, annealed at 723 K for 100 h
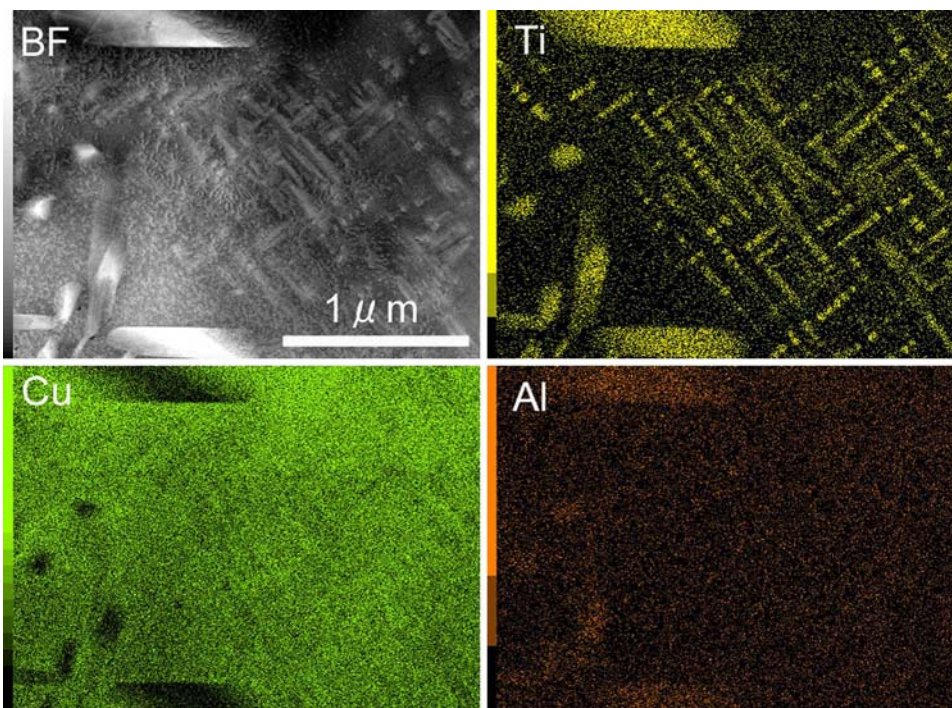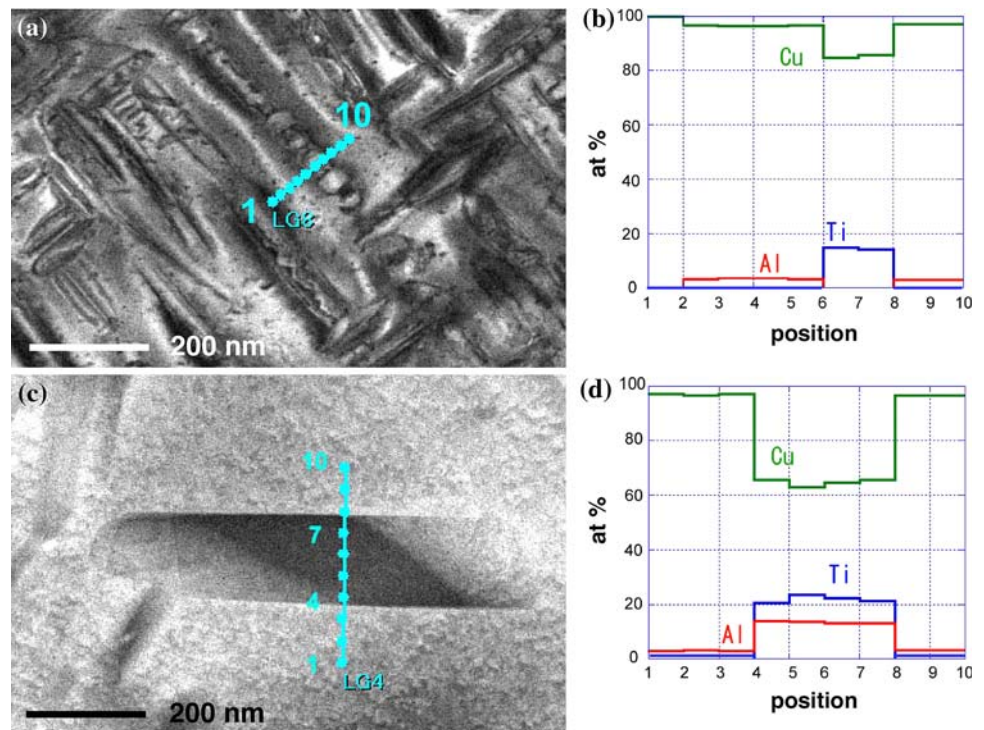
Fig. 7 (a) STEM–BF images and (b) characteristic X-ray intensity profiles of the α-Cu$_4$Ti precipitate; (c) and (d) the AlCu$_2$Ti precipitate

diffraction spots, we suspect that the contrasts originate from highly coherent clusters formed by the alloying elements, analogous to the G.P. zones [19–21]. The characteristic appearance of contrasts, which were found parallel to {110} planes of Cu, also support this view. Then, we are led to propose that the formation of these clusters resulted in the decrease of chemical potential of Ti, which in return prevented the system to decompose spinodally. It is also interesting to point out that the modulation length observed for the Cu–3 at.%Ti alloy was approximately 4 nm [7].

In any case, we must conclude that the α-Cu$_4$Ti precipitates form via nucleation and growth mechanism in the ternary Cu–3 at.%Ti–4 at.%Al alloy. The size of each precipitate was approximately 50 nm in length, which compares favorably with 3–5-nm thick and 40-nm long α-Cu$_4$Ti precipitates reported earlier for the peak-aged Cu–3 at.%Ti alloy [7]. Thus, the decrease in strength of the ternary alloy is not due to the size of the precipitates, but due to the relatively small number density. It is also interesting to point out that the size of α-Cu$_4$Ti precipitates in the over-aged alloys at 723 K is about 100 nm in length for both the binary and ternary systems.

As for the conductivity, two effects need to be taken into account: the distribution of the secondary phase; and the solubility of Ti in the conducting Cu matrix. The former was just described above, which presumably resulted in the improvement of conductivity of the ternary alloy. The latter is difficult to access. For example, the available

literatures on the Cu–Ti–Al alloy system show that the solubility limit of Ti in Cu does not vary systematically with temperature when Al is added [14]. Nevertheless, since the fcc Cu phase is in equilibrium with the α-Cu$_4$Ti phase (and with the AlCu$_2$Ti in the case of the ternary system), we may conclude that the terminal fcc Cu solutions in the over-aged alloys must contain Ti (and Al) to their respective solubility limits. Then, the fact that the conductivity did improve considerably in the ternary alloy suggests that the amount of solute Ti probably decreased by the addition of Al. The characteristic X-ray line profiles shown in Fig. 7 also seem to support this view, although it is true that further studies are definitely needed to elucidate the effect of solute Al on the Ti solubility in Cu.

The α-Cu$_4$Ti precipitates exhibit a distinct square rod morphology. Both the SAD pattern obtained from single rod, and the moiré pattern (Fig. 4) indicated that the long axis of the rod is in fact along the c-axis of the tetragonal α-Cu$_4$Ti phase. Since the tetragonal phase expands in the a directions by 2%, it is energetically favorable when it grows in the c direction. On the other hand, the edges of the square are parallel to the {100} planes, as shown clearly in the STEM images (Fig. 4). This means that the interfacial energy between the α-Cu$_4$Ti and fcc Cu does depend on habit planes, and that it is minimum for {100}. With these observations, we can summarize that the square rod shape is the result of the minimization of the interfacial energy of, and the strain energy created by, the tetragonal α-Cu$_4$Ti phase.
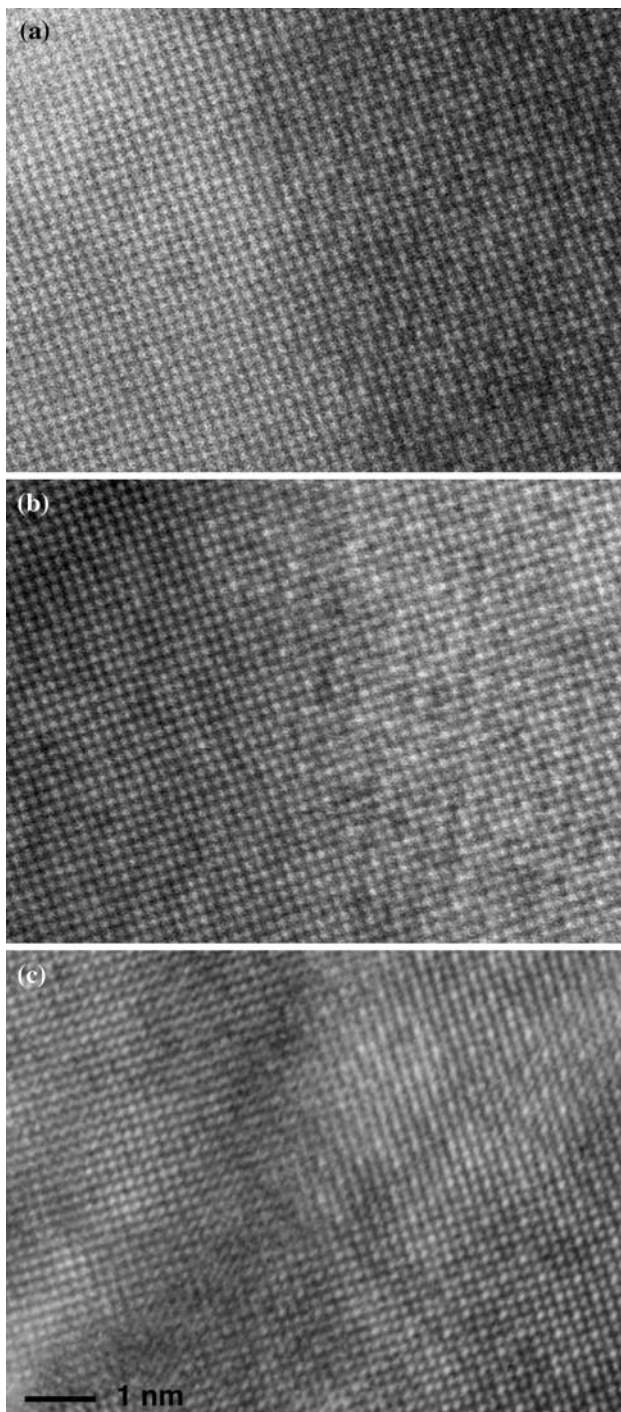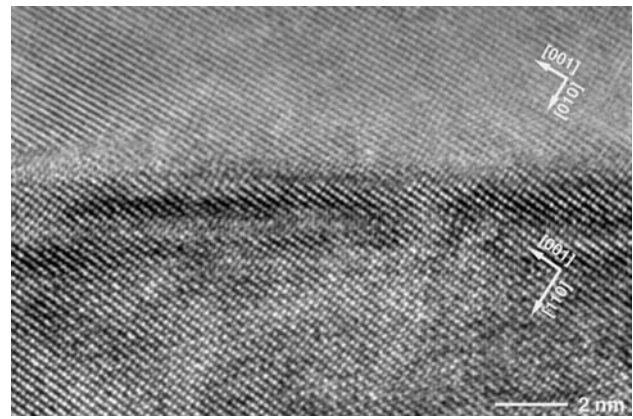
Fig. 9 HRTEM image taken from the interface region of the $AlCu_2Ti$ precipitate (lower) and the Cu matrix (upper). The image was taken along the $[1\bar{1}0]$ zone axis of the precipitate. The angle between the [001] of Cu and [001] of the $AlCu_2Ti$ precipitate is about 7°. Note the presence of misfit dislocations, which can be viewed at a glancing angle

Finally, we found that the ternary $AlCu_2Ti$ phase also precipitated in such a way so as to lower the lattice mismatch (Fig. 9). First, the habit plane was found to be not exactly but close to the {110} planes of the Cu matrix. Second, the OR between the matrix and the precipitate was not uniquely determined in this study, but the following information has been obtained. Namely, the 100 pole of the matrix and $1\bar{1}0$ pole of the precipitate are apart from each other by about 5°; and the projected image onto the 110 plane showed that the angle between the 001 axis of the fcc Cu phase and that of the $AlCu_2Ti$ phase was approximately 7°. Since the interplanar spacing of {220} and {004} planes of the $AlCu_2Ti$ phase is 0.212 and 0.150 nm, respectively, which should be compared with 0.181 nm, the {200} spacing of the fcc Cu, some optimization has to be made to compensate for the lattice mismatch. Looking at Fig. 9 from the glancing angle along the [001] axis of the $AlCu_2Ti$ phase, one can observe that there exist misfit dislocations as mentioned earlier. This is in fact also true along the [110] axis of the ternary phase. Thus we may state that the $AlCu_2Ti$ phase also precipitates and grows according to the interfacial minimization principle. For further improvement of the mechanical and electrical properties of Cu–Ti–Al alloys, an optimization of the Al content and annealing conditions seems necessary.

Fig. 8 Atomic resolution (**a**) STEM–HAADF, (**b**) STEM–BF, and (**c**) HRTEM images obtained from an interface region of the Cu matrix (left) and the α-Cu_4Ti precipitate (right). ((**a**) and (**b**) were obtained simultaneously from exactly the same region, while (**c**) was obtained from another region.) Note that Ti atomic columns appear darkest in (**a**) and brightest in (**b**), whereas Cu atomic columns appear bright in both (**a**) and (**b**). Note also the similarity of contrasts between (**b**) and (**c**), demonstrating the reciprocity principle

Conclusions

We have examined aging behaviors of ternary Cu–3 at.% Ti–4 at.%Al alloy annealed at 723 K, and compared them

with those of binary Cu–3 at.%Ti alloy. Our results can be summarized as follows.

(1) The ternary alloy exhibited the peak hardness of 180 Hv after 2 h anneal, which can be compared with 280 Hv after 8 h, the value obtained for the binary alloy.

(2) Conductivity reached 6%IACS after 2–4 h anneal, which is about six times better than the binary alloy.

(3) As-quenched alloy does not decompose spinodally, but coherent clusters of about 4 nm were found to form on {110} planes of the Cu matrix.

(4) The major hardening precipitate is the α-Cu_4Ti phase, which grows via nucleation and growth mechanism, as compared with spinodal decomposition operating in the binary Cu–3 at.%Ti alloy.

(5) The precipitates grow in the c direction of the tetragonal unit cell to minimize the strain energy, resulting in the square rod shape of approximately 50 nm in length.

(6) The $AlCu_2Ti$ phase ($D0_3$) also precipitates with the major habit plane close to {110} of the fcc Cu matrix, while the OR was not determined conclusively, but it was found that the 100 and 110 poles of the matrix and precipitates, respectively, are about 5° apart, and the angle between their 001 axes is close to 7°.

References

1. Rioya RJ, Laughlin DE (1980) Acta Metall 28:1301
2. Yamamoto A, Tsubakino H (1994) Script Metall Mater 31:787
3. Nagarjuna S, Sarma DS (2002) J Mater Sci 37:1929
4. Suzuki S, Hirabayashi K, Shibata H, Mimura K, Isshiki M, Waseda Y (2003) Scripta Mater 48:431
5. Soffa WA, Laughlin DE (2004) Prog Mater Sci 49:347
6. Hernandez-Santiago F, Cayetano-Castro N, Lopez-Hirata VM, Dorantes-Rosales HJ, Cruz-Rivera JJ (2004) Mater Trans 45:2312
7. Nishio R, Konno TJ, Semboshi S (2005) Mater Sci Forum 502:163
8. Massalski TB (ed) (1990) Binary alloy phase diagrams, 2nd edn. ASM International, Materials Park, p 1494
9. Pfeifer HU, Bahn S, Schubert K (1968) J Less-Common Met 14:291
10. Brun J-Y, Hamar-Thibault S-J, Allibert C-H (1983) Z Metallkde 74:525
11. Knights R, Wilkes P (1973) Acta Metall 21:1503
12. Borchers C (1999) Phil Mag A 79:537
13. Nishio R (2006) MSc thesis, Osaka Prefecture University
14. Ran Q, Stadelmaier HH (1992) In: Petzow G, Effenberg G (eds) Ternary alloys. VCH, Materials Park, p 51
15. Raman A, Schubert K (1965) Z Metalknd 56:99
16. Reimer L (1993) Transmission electron microscopy. Springer–Verlag, Berlin
17. Laughlin DE, Cahn JW (1975) Acta Metall 23:329
18. Datta A, Soffa WA (1976) Acta Metall 24:987
19. Guinier A (1938) Nature 142:569
20. Preston GD (1938) Nature 142:570
21. Konno TJ, Kawasaki M, Hiraga K (2001) Phil Mag B 81:1713